ISSN 0016-7037
Volume 75, Number 13
July 1, 2011

ELSEVIER

Geochimica et Cosmochimica Acta

JOURNAL OF THE GEOCHEMICAL SOCIETY AND THE METEORITICAL SOCIETY

Volume 75, Number 13 July 1, 2011

Articles

Continued on outside back cover

Available online at www.sciencedirect.com

ScienceDirect

Geochimica et Cosmochimica Acta 75 (2011) 3792–3802

Geochimica et Cosmochimica Acta

www.elsevier.com/locate/gca

First principles molecular dynamics simulations of diopside ($CaMgSi_2O_6$) liquid to high pressure

Ni Sun [a], Lars Stixrude [b,*], Nico de Koker [c], Bijaya B. Karki [d,e]

[a] Department of Geological Sciences, University of Michigan, Ann Arbor, MI 48109, USA
[b] Department of Earth Sciences, University College London, London, WC1E 6BT, UK
[c] Bayerisches Geoinstitut, Universität Bayreuth, Germany
[d] Department of Computer Science, Louisiana State University, Baton Rouge, Louisiana 70803, USA
[e] Department of Geology and Geophysics, Louisiana State University, Baton Rouge, Louisiana 70803, USA

Received 6 July 2010; accepted in revised form 7 April 2011; available online 13 April 2011

Abstract

We use first principles molecular dynamics simulations based on density functional theory in the local density approximation to investigate $CaMgSi_2O_6$ liquid over the entire mantle pressure regime. We find that the liquid structure becomes much more densely packed with increasing pressure, with the mean Si–O coordination number increasing nearly linearly with volume from fourfold near ambient pressure to sixfold at the base of the mantle. Fivefold Si–O coordination environments are most abundant at intermediate compression. The properties of Mg and Si coordination environments are nearly identical to those in $MgSiO_3$ liquid, whereas Ca is more highly coordinated with larger mean Ca–O bond length as compared with Mg. The density increases smoothly with increasing pressure over the entire range studied. The Grüneisen parameter increases by a factor of three on twofold compression. The density contrast between diopside composition liquid and the isochemical crystalline assemblage is less than 2% at the core mantle boundary, less than that in the case of $MgSiO_3$. Thermodynamic properties are described in terms of a liquid-state fundamental thermodynamic relation.

1. INTRODUCTION

Knowledge of silicate liquids over the large range of pressure and temperature in Earth's mantle is important to understand magma generation and transport, as well as the chemical and thermal evolution of Earth. Although most of the mantle is solid, several lines of evidence point to the important role of silicate liquids over the entire mantle pressure regime including evidence from xenoliths (Haggerty and Sautter, 1990), the origin of komatiites (Miller et al., 1991; Herzberg, 1995), seismic observations of ultra low velocity zone (ULVZ) at the core mantle boundary (136 GPa, 2890 km depth) (Williams and Garnero, 1996), and giant-impact models of lunar formation (Canup, 2004), which predict a largely or completely molten early Earth.

Recent models of a crystallizing magma ocean have highlighted the importance for the Earth's earliest evolution of some basic properties of silicate liquids at high pressure, including the density contrast with respect to coexisting solids, and the isentropic temperature gradient (Labrosse et al., 2007). Here, we focus on diopside ($CaMgSi_2O_6$) composition liquid, which is a major component of basalt, and of the lower mantle: the sub-solidus phases $MgSiO_3$ perovskite and $CaSiO_3$ perovskite, make up more than 80% of the lower mantle. Diopside liquid has been studied extensively in the laboratory at ambient pressure where its thermodynamic properties are well characterized (Stebbins et al., 1984; Lange, 1997; Ai and Lange, 2008). However, most studies were performed at ambient pressure and measurements above 40 GPa consist of only two shock wave points (Asimow and Ahrens, 2010). The properties of

* Corresponding author. Tel.: +44 (0)20 7679 7929.
E-mail address: l.stixrude@ucl.ac.uk (L. Stixrude).

0016-7037/$ - see front matter
doi:10.1016/j.gca.2011.04.004

diopside composition liquid throughout most of the mantle pressure regime remain uncertain, leaving important questions open, such as the relative density of Ca-bearing silicate liquids with respect to co-existing solids.

In this study, we investigate diopside liquid across the entire mantle pressure–temperature regime by first principles molecular dynamics (FPMD) simulations, which have been successfully used to study other silicate liquids. Diopside liquid has not been studied by this method before. Previous molecular dynamics simulations of CaO–MgO–SiO_2 liquids have been based on semi-empirical interionic potentials (Angell et al., 1987; Matsui, 1996; Zhang et al., 2010). The advantage of FPMD is that it is non-empirical, thereby allowing predictions that are independent of experiment and which, as shown in previous FPMD studies on silicate liquids, agree very well with experimental measurements (Stixrude and Karki, 2005; de Koker et al., 2008; Mookherjee et al., 2008; de Koker, 2010). We investigate the thermodynamic properties and structure of the liquid. We compare our first principles results to extant experimental data and predict properties at conditions beyond those of current experiments. Our simulations also provide an opportunity to investigate the influence of Ca on silicate liquid structure. To this end, we compare our results to previous simulations of $MgSiO_3$ liquid to examine the effect of the larger Ca cation on local coordination environments and on network connectivity.

2. THEORY

Following our previous work (Stixrude and Karki, 2005), our simulations are based on density functional theory (DFT) (Kohn, 1999) in the local density approximation (LDA) (Ceperley and Alder, 1980) and the plane-wave pseudopotential method. For comparison, we also perform a limited number of calculations in the generalized gradient approximation (GGA). All calculations were performed with the Vienna ab initio simulation package (VASP) (Kresse et al., 1992; Kresse and Furthmuller, 1996). We computed the electronic structure and forces at the Brillouin zone center with an energy cutoff, $E_{cut} = 400$ eV.

All molecular dynamics simulations in this study were performed for an 80-atom cubic unit cell. As in our previous work, Born-Oppenheimer simulations are performed in the canonical ensemble with a Nosé thermostat (Nosé, 1984) and a time step of 1 fs. We assume thermal equilibrium between ions and electrons via the Mermin functional (Mermin, 1965; Wentzcovitch et al., 1992). We note that Born-Oppenheimer molecular dynamics, while somewhat more expensive than Car–Parinello dynamics (Car and Parrinello, 1985; Wan et al., 2007), is in principle more robust: inaccuracies in Car–Parinello dynamics have been claimed in systems with conduction electrons (Vorberger et al., 2007), such as occur at the high temperature limit of our simulations in other oxide liquids (Karki et al., 2006). The initial condition is a pyroxene supercell homogeneously strained to a cubic shape. The system is melted at 6000 K, then isochorically cooled to 4000, 3000, and 2000 K. For each calculation, the total run duration is 8 ps, with the last 6.4 ps used to compute equilibrium properties. Convergence tests, including larger systems (160 atoms), and longer runs (11 ps) produced results within the statistical uncertainty of our simulations. The volumes we explored range from $V = V_X$ to $V = V_X/2$, where $V_X = 81.8\ \mathrm{cm}^3/\mathrm{mol}$.

Pressure is reported as (de Koker et al., 2008)

$$P(V,T) = P_{MD}(V,T) + P_{Pulay}(V) + P_{xc} \quad (1)$$

where P_{MD} is the pressure from the FPMD simulation, P_{Pulay} is the Pulay (finite basis set) correction (Francis and Payne, 1990), and P_{xc} is the semi-empirical correction for systematic bias in the approximation to the exchange-correlation potential (LDA or GGA). As in our previous work, we compute the Pulay term as

$$P_{Pulay}(V) = P(V; E_{cut} = 600\ \text{eV}) - P(V; E_{cut} = 400\ \text{eV}) \quad (2)$$

on a series of liquid snapshots. We find that the Pulay term varies nearly linearly with volume from 2.3 GPa at $V = V_X$ to 4.7 GPa at $V = V_X/2$ and that it is essentially identical in LDA and GGA.

The motivation for the semi-empirical correction is the finding that LDA systematically, and by a small amount, overbinds as shown by previous studies of crystalline silicates and oxides (Karki et al., 2001), and many other systems (van de Walle and Ceder, 1999). Van de Walle and Ceder (1999) noticed that LDA and experimental equations of state nearly coincide upon the addition of a small uniform pressure correction, an observation that we have confirmed in our previous studies of silicates and oxides (de Koker and Stixrude, 2009). We follow this procedure here and compute the correction as (de Koker et al., 2008)

$$P_{xc} = -P_{VASP}(V_{xtl}) \quad (3)$$

where P_{VASP} is the pressure computed by VASP for the fully relaxed static structure of crystalline diopside (20 atom primitive unit cell, spacegroup $C2/c$), and $V_{xtl} = 65.23(6)\ \mathrm{cm}^3\ \mathrm{mol}^{-1}$ is the experimental zero-pressure volume of crystalline diopside at static conditions, computed via the thermodynamic model of (Stixrude and Lithgow-Bertelloni, 2005) and uncertainty computed via formal error propagation. The values obtained for LDA: $P_{xc} = 2.5(2)$ GPa, and GGA: $P_{xc} = -5.3(2)$ GPa are consistent with the well-known over-binding tendency of LDA, and under-binding tendency of GGA and are similar in magnitude to previous estimates (Oganov et al., 2001; Stixrude and Karki, 2005). We have also added a correction to the internal energy as demanded by thermodynamic consistency: $E_{xc}(V) = -\int_{V_0}^{V} P_{xc}(V)dV$, (de Koker and Stixrude, 2009).

The thermodynamic properties of the melt are analyzed according to the fundamental relation recently proposed (de Koker and Stixrude, 2009, 2010). Briefly, the functional form is specified by the Helmholtz free energy

$$F = F_{xs} + F_{ig} + F_{el} \quad (4)$$

where the first term is the excess term

$$F_{xs}(V,T) = \sum_{i=0}^{O_f'} \sum_{j=0}^{O_\theta'} \frac{a_{ij}}{i!j!} f^i \theta^j \quad (5)$$

where f is the Eulerian finite strain

$$f = \frac{1}{2}\left[\left(\frac{V}{V_0}\right)^{-2/3} - 1\right] \tag{6}$$

the thermal function

$$\theta = \left[\left(\frac{T}{T_0}\right)^{m} - 1\right] \tag{7}$$

values of the a_{ij} and m are determined by fitting the FPMD results and the primes on the limits of the summations indicate that $i + j < 4$. The a_{ij} are related to thermodynamic properties at the reference state (V_0, T_0): the volume, isothermal bulk modulus K_T, its pressure derivative K', the Helmholtz free energy, entropy S, the thermal pressure coefficient

$$\alpha K_T = \left(\frac{\partial P}{\partial T}\right)_V \tag{8}$$

and its volume derivative, where α is the thermal expansivity, as shown in the appendix to de Koker and Stixrude (2009). The ideal gas contribution

$$F_{ig} = -k_B T \sum_i N_i \ln\left(\frac{eq_i}{N_i}\right) \tag{9a}$$

$$q_i = \frac{V}{\Lambda_i^3} \sum_j \omega_{ij} e^{-\varepsilon_{ij}/k_B T} \tag{9b}$$

where the sums are respectively over atom types i, and excited electronic states j, N_i is number of atoms of type i, Λ_i is the de Broglie thermal wavelength, k_B is the Boltzmann constant, e is the base of the natural logarithm, i.e. $\ln e = 1$, and ω_{ij} and ε_{ij} are respectively the degeneracy and energy of the jth electronic level (Ralchenko et al., 2010). We recover the familiar Sackur–Tetrode equation for the entropy of the ideal gas via the thermodynamic identity $S_{ig} = -(\partial F_{ig}/\partial T)_V$ (Atkins, 1994, p. 686). The electronic contribution

$$F_{el} = -\zeta T^2\left[\frac{1}{2}\left(1 - x_{el}^2\right) - x_{el}\ln x_{el}\right] \tag{10}$$

and $F_{el} = 0$ for $x_{el} > 1$, where $x_{el} = T_{el}/T$, the electronic heat capacity coefficient $\zeta = \zeta_0(V/V_0)^{\xi}$ and the onset temperature for thermoelectronic effects $T_{el} = T_{el0}(V/V_0)^{\eta}$.

The procedure used to determine the values of the coefficients is described in detail in de Koker and Stixrude (2009). Briefly, we first determine the values of the electronic parameters T_{el}, ζ_0, ξ, and η by performing a least squares fit to the FPMD results for the electronic entropy $S_{el} = -dF_{el}/dT$ with F_{el} given by Eq. (10). We then determine the values of the coefficients a_{ij} and m via a least-squares fit to the excess part of the pressure: $P_{XS} = P_{FPMD} - P_{ig} - P_{el}$, and internal energy: $E_{xs} = E_{FPMD} - E_{ig} - E_{el}$, where ideal gas and electronic contributions, computed respectively from Eqs. (9) and (10), are subtracted from the values determined from the FPMD simulations.

Once the coefficients are determined by fitting to the FPMD results, all equilibrium thermodynamic properties may be computed by taking volume and temperature derivatives of (4). In this study, we also examine the isochoric heat capacity

$$C_V = \left(\frac{\partial E}{\partial T}\right)_V \tag{11}$$

and the Grüneisen parameter

$$\gamma = V\left(\frac{\partial P}{\partial E}\right)_V \tag{12}$$

The Hugoniot is found as the set of state points that satisfy the Rankine–Hugoniot equation

$$E_H - E_0 = \frac{1}{2}(V_0 - V_H)P_H \tag{13}$$

where E_H, P_H, and V_H are the internal energy, pressure, and volume in the shocked state; E_0 and V_0 are the internal energy and volume at ambient pressure and the pre-shocked temperature. E_0 and V_0 are computed from our FPMD simulations and solutions to Eq. (13) are found self consistently using the fundamental relation (Eq. (4)). The procedure follows many previous studies including our own (de Koker and Stixrude, 2009): at a given volume, V_H, and knowing the variation of E and P with temperature at V_H from our FPMD simulations, we find the temperature T_H such that Eq. (13) is satisfied. The Hugoniot temperature T_H then represents an additional prediction of our theoretical calculations.

We report values of the following structural quantities (McQuarrie, 1976): $R_{\alpha\beta}$ the most probable bond distance between atom types α and β as measured by the position of the first peak in the corresponding partial radial distribution function $g_{\alpha\beta}(r)$,

$$\langle r\rangle = \frac{\int_0^{r_{\alpha\beta}^{\min}} r^3 g_{\alpha\beta}(r)dr}{\int_0^{r_{\alpha\beta}^{\min}} r^2 g_{\alpha\beta}(r)dr} \tag{14}$$

the mean separation over the first coordination shell, and

$$Z_{\alpha\beta} = 4\pi\rho x_\beta \int_0^{r_{\alpha\beta}^{\min}} r^2 g_{\alpha\beta}(r)dr \tag{15}$$

the coordination number, where $r_{\alpha\beta}^{\min}$ is the distance to the first minimum in $g_{\alpha\beta}$, ρ is the atomic number density and x_β is the number fraction of atom type β. We characterize the network connectivity by Q^n, the proportion of Si atoms linked through bridging oxygens to n other Si atoms. The distribution of Q species is summarized by

$$k_n = \left[Q^{n-1}\right]\left[Q^{n+1}\right]/\left[Q^n\right]^2 \tag{16}$$

the equilibrium constants of the reaction $2Q^n = Q^{n-1} + Q^{n+1}$ $(1 < n < 3)$ (Stebbins, 1987).

3. RESULTS

3.1. Structure

The liquid structure at $V = V_X$ agrees well with existing experimental data including cation-oxygen coordination numbers, bond lengths and Q speciation (Table 1). Bond lengths reported from X-ray diffraction studies on $MgSiO_3$ and $CaSiO_3$ liquids (Waseda and Toguri, 1977) fall in between computed values of the most probable and mean bond lengths. The most probable and mean bond lengths

Table 1
Comparison of theoretical structure of diopside liquid at $V = V_X$ and $T = 3000$ K to experimentally determined structural parameters on $(Mg_xCa_{1-x})_2Si_2O_6$ glasses and liquids. In addition to the mean bond distance $\langle r \rangle_{\alpha\beta}$ (Eq. (14)), we also report $R_{\alpha\beta}$ in parentheses. Uncertainties in Q^n and k_n are given in parentheses for the last digits reported.

	Theory	Experiment	T (K)	x	
Z_{Si-O}	4.06	3.9, 3.9	1973, 1873	0, 1	Waseda and Toguri (1977)
Z_{Mg-O}	4.87	4.3	1973	0	
Z_{Ca-O}	5.89	5.7	1873	1	
R_{Si-O}, $\langle r \rangle_{Si-O}$ (Å)	1.622, 1.688	1.63, 1.63	1973, 1873	0, 1	
R_{Mg-O}, $\langle r \rangle_{Mg-O}$ (Å)	1.974, 2.212	2.16	1973	0	
R_{Ca-O}, $\langle r \rangle_{Ca-O}$ (Å)	2.243, 2.505	2.41	1873	1	
Q^0 (%)	1.5 (8)	0.0	300	0.5	Schneider et al. (2000)
Q^1 (%)	22.8 (38)	28 (8)	300	0.5	
Q^2 (%)	38.7 (30)	43 (10)	300	0.5	
Q^3 (%)	19.1 (7)	25 (6)	300	0.5	
Q^4 (%)	6.9 (15)	4 (1)	300	0.5	
k_1	0.11 (8)	0	300	0.5	
k_2	0.29 (7)	0.38 (23)	300	0.5	
k_3	0.73 (17)	0.28 (37)	300	0.5	

differ because of the asymmetry in the first peak in the radial distribution function (McQuarrie, 1976). This asymmetry is not taken into account in the analysis of the experimental data, in which bond lengths are modeled assuming a Gaussian distribution of bond lengths. The asymmetry of the first peak also likely accounts for the experimental coordination numbers being slightly smaller than those predicted theoretically.

Liquid structure changes substantially on compression, becoming much more efficiently packed by increasing cation-oxygen coordination numbers (Figs. 1 and 2). Cation-oxygen coordination numbers all increase monotonically and smoothly on compression, reaching values of 6 (Si–O), 8 (Mg–O) and 10 (Ca–O) at $V = V_X/2$. The Si–O bond distance initially increases on compression before decreasing with further compression for $V/V_X < 0.65$. The Mg–O and Ca–O bond distances decrease on compression over most of the range studied, but are insensitive to compression near $V = V_X$.

At all volumes, the Mg–O and Si–O coordination environments are similar to that in $MgSiO_3$ composition liquid, whereas the Ca–O coordination environment is characterized by a larger coordination number and larger bond distance, consistent with the larger ionic radius of Ca as compared with Mg.

Increasing temperature at constant volume has little effect on the mean coordination numbers but does influence the distribution of coordination environments (Fig. 2). Heating tends to produce a wider variety of coordination environments. For example, at $V = V_X$, odd Si–O coordination environments (3- and 5-fold) make up less than 10% of the total at 3000 K, and 50% at 6000 K. The proportion of fivefold coordinated Si initially increases on compression at the expense of fourfold, and then decreases upon further compression as sixfold coordination becomes most abundant; at intermediate compressions ($V/V_X = 0.7$) fivefold coordination is the most abundant. The O–Si coordination distribution at $V = V_X$ is nearly identical to that in pyroxene in which 2/3 of the oxygens are onefold coordinated (non-bridging oxygens) and 1/3 are twofold coordinated (bridging oxygens). On compression twofold coordination increases at the expense of onefold, and oxygen tri-clusters (O bonded to 3 Si) also increase.

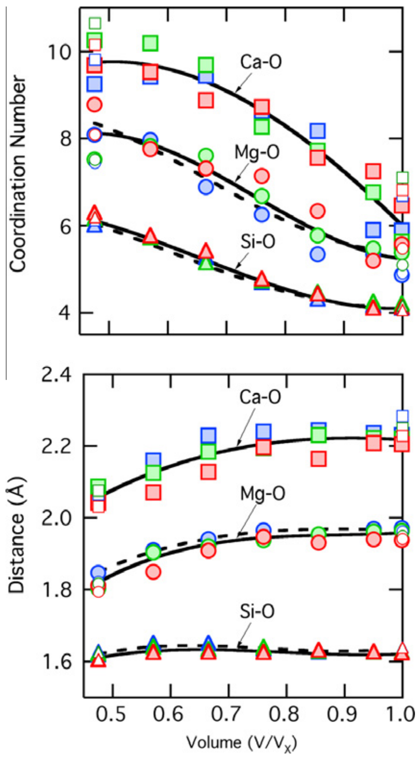

Fig. 1. (top) Mean cation-oxygen coordination numbers and (bottom) bond distances in $CaMgSi_2O_6$ liquid at 3000 K (blue), 4000 K (green), and 6000 K (red). The dashed lines show the temperature-averaged trends for $MgSiO_3$ liquid (Stixrude and Karki, 2005). (For interpretation of the references to colour in this figure legend, the reader is referred to the web version of this article.)

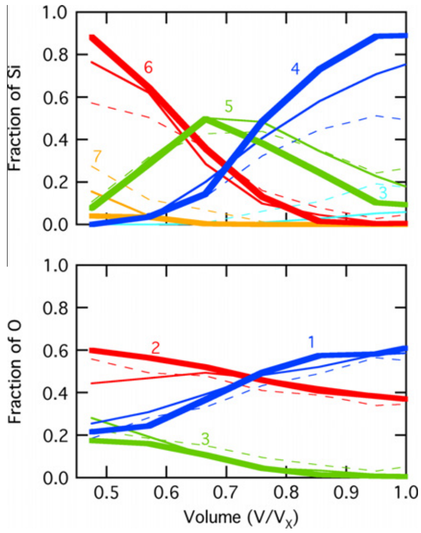

Fig. 2. Si–O (top) and O–Si (bottom) coordination distribution in $CaMgSi_2O_6$ liquid at 3000 K (bold), 4000 K (thin solid), and 6000 K (dashed).

GGA yields structural quantities that are nearly identical to LDA (Fig. 1), with the possible exception of Z_{Ca-O}, and R_{Ca-O} at low pressure, which are slightly larger in GGA than in LDA.

3.2. Equation of state

We found that the series (Eq. (5)) truncated at $O_f = 3$ and $O_\theta = 1$ adequately captures the FPMD results, and matches simulated values of the pressure, internal energy, and electronic entropy nearly to within simulation uncertainty (Fig. 3). This choice corresponds to a third order Birch–Murnaghan equation of state for the reference isotherm, and the lowest order expansion in the thermal variable θ. The parameters of the fundamental relation are specified in Table 2. Higher order expansions of course produce a slightly better fit to the FPMD results (*cf.* the deviation between the fit and the mean C_V at the highest compression), but at the cost of many more parameters with larger uncertainty.

The pressure and internal energy vary smoothly with volume throughout the pressure range studied (Fig. 3 and Table 3). On compression, the influence of temperature on the pressure increases, while the influence of temperature on the internal energy decreases slightly. These patterns are reflected in the increase of the thermal pressure coefficient and the Grüneisen parameter and the decrease in the heat capacity on compression. The FPMD results for pressure, energy, enthalpy, and electronic entropy are listed with their uncertainties in Table 3.

The properties of the liquid derived from the FPMD simulations agree well with extant experimental data (Table 4). The variation of the pressure at $V = V_X$ is consistent with the experimental measurements of the thermal expansivity and bulk modulus (Fig. 3 top left inset). The FPMD volume at $P = 0$ and $T = 1773$ K is slightly overestimated and this likely accounts for the fact that the FPMD bulk moduli are slightly underestimated and the thermal expansivity overestimated. These discrepancies may also be due, at least in part, to uncertainties in the extrapolation of the FPMD results to the lower temperatures of the experiments.

Many thermodynamic properties are essentially identical in GGA and LDA, including the heat capacity, thermal pressure coefficient, Grüneisen parameter, and electronic entropy (Fig. 3). While differences in derivatives are subtle, the absolute total energy is systematically offset in GGA as compared with LDA, which reflects energetic contributions from tightly bound states that have little influence on thermodynamic properties. The pressure differs systematically between the two approximations. The pressure in GGA is uniformly higher than it is in LDA. Upon addition of P_{xc}, GGA pressures are systematically lower than those in LDA at $V = V_X$, and systematically higher at $V/V_X = 0.5$. Upon addition of P_{xc}, GGA predicts a zero pressure volume of diopside liquid that is smaller than experimentally measured: the corrected GGA pressure at $V = V_X$, extrapolated to 1773 K is less than −4 GPa (Fig. 3 inset).

The predicted Hugoniot agrees very well with existing shock wave data from a molten initial state, including two new high pressure points at $P > 75$ GPa (Asimow and Ahrens, 2010; Rigden et al., 1989) (Fig. 4). In the experimental studies Hugoniot temperature was not measured. Our FPMD Hugoniot temperatures are substantially higher than those computed by Rigden et al. (1989) on the basis of a thermodynamic model: whereas the temperature at 38 GPa was estimated to be 2076(170) K in the experimental study, we find 3000 K. The reason for this discrepancy is the approximate model for the volume dependence of the Grüneisen parameter adopted in the experimental study. Whereas Rigden et al. (1989) assumed that the Grüneisen parameter of the liquid decreased on compression, we find it to increase, which produces more rapid heating on the Hugoniot. We present our predictions for the longitudinal wave velocity v_P of the liquid as it is important for evaluating the seismic signature of melt in the deep Earth (Stixrude et al., 2009) and because it may be possible also to measure this quantity experimentally in the future, providing an additional test of our predictions.

We have also compared to Hugoniot data from a crystalline initial state (diopside) at ambient conditions (Svendsen and Ahrens, 1983, 1990). At the highest pressure the data fall at significantly lower density and higher temperature than our predicted liquid-phase Hugoniot. We suggest based on this comparison, that the experimental study is in a mixed phase regime and that complete melting was not achieved. To explore this further, we also show Hugoniots computed for diopside and high-pressure isochemical crystalline assemblages. The highest pressure experimental point lies, to within uncertainty, in between our calculated Hugoniot for the liquid state and that for an equimolar mixture of $CaSiO_3$ and $MgSiO_3$ perovskite, suggesting that this point is still partially molten.

The density contrast between diopside liquid and the isochemical crystalline assemblage decreases rapidly with increasing pressure (Fig. 5). The contrast vanishes at 14 GPa on the 2428 K isotherm, nearly coinciding with

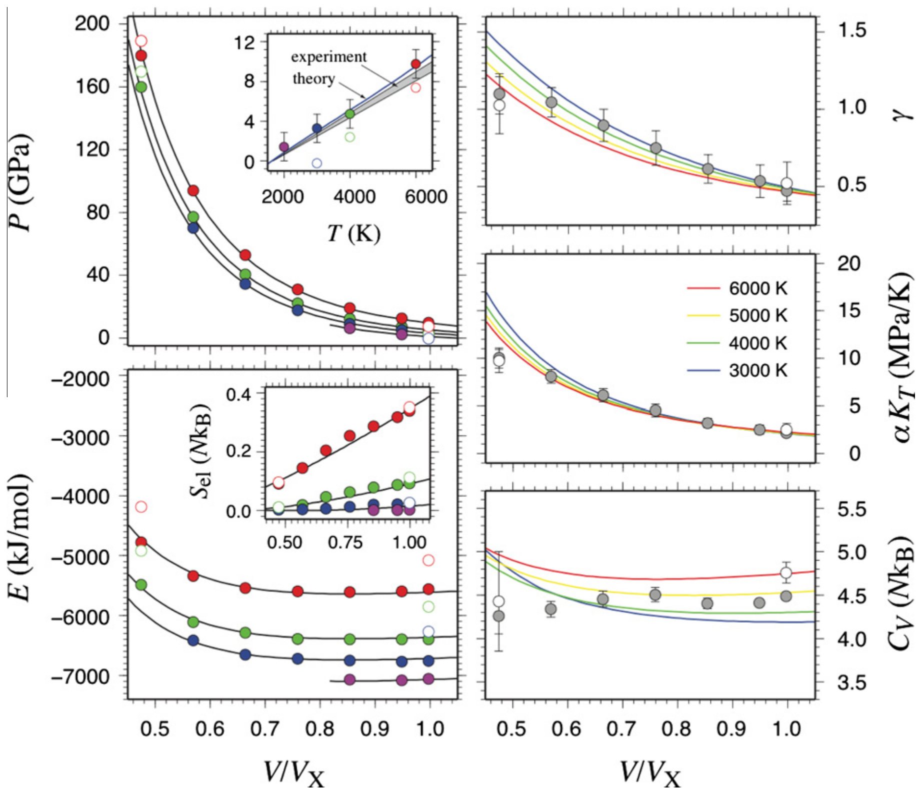

Fig. 3. (top left) Equation of state of $CaMgSi_2O_6$ liquid showing FPMD results (circles) at 2000 K (purple), 3000 K (blue), 4000 K (green), and 6000 K (red) and the inset showing pressure vs. temperature at $V = V_X$ compared with experimentally based extrapolation (shading) (Ai and Lange, 2008; Lange, 1997). (bottom left) Internal energy from FPMD and the inset showing the FPMD electronic entropy. (right column from top to bottom) Grüneisen parameter γ, thermal pressure coefficient αK_T where α is the thermal expansivity and K_T is the isothermal bulk modulus, and the heat capacity C_V with symbols indicating the mean FPMD values at each volume over the temperature range 3000–6000 K. In all figures, filled symbols indicate LDA results, open symbols indicate GGA results; in both cases the semi-empirical exchange-correlation correction has been applied (see text). In all figures, lines are computed from the fundamental relation discussed in the text and in the right column colored to indicate temperature as indicated. (For interpretation of the references to colour in this figure legend, the reader is referred to the web version of this article.)

Table 2
Specification of the excess portion of the FPMD fundamental relation of diopside liquid. The reference state is $P = 0$ GPa, $T = 3000$ K, the thermal exponent $m = 0.614$, and the electronic term is specified by $T_{el} = 1859$ K, $\zeta_0 = 0.01982$, $\xi = 0.602$, $\eta = -0.596$.

V_0 (cm^3/mol)	K_{Tsx0} (GPa)	K'_{Tsx0}	F_{xs0} (kJ mol^{-1})	S_{xs0} (J mol^{-1} K^{-1})	αK_{Txs0} (GPa K^{-1})	$V\,(d\alpha KT/dV)_{xs0}$ (MPa K^{-1})
97.24	7.55	8.24	−5576	−491	0.479	−2.562

the melting curve of diopside and accounting for the vanishing dT/dP Clapeyron slope of melting at that pressure (Gasparik, 1996). At 4000 K, the density contrast remains positive (crystals denser) throughout the mantle pressure regime, but at the base of the mantle it approaches very small values of less than 2%.

4. DISCUSSION

At first glance it may appear remarkable that the liquid structure in our simulations performed at 3000 K agrees with that experimentally measured at lower temperatures. In fact, we find that mean structural parameters, such as $Z_{\alpha-\beta}$ and $R_{\alpha-\beta}$ depend little on temperature at constant volume, particularly at large volume (Fig. 1). The agreement with experiment is therefore not surprising in the context of our results. This emphasizes the primary role of volume, rather than pressure or temperature in controlling liquid structure. We expect liquid structure to vary more on isobaric heating, the usual experimental situation, than on isochoric heating. At constant pressure, heating causes the volume to increase, and we expect the structure to change because of this thermal expansion. This notion has potentially important implications for detailed comparison of the structure of glasses at ambient conditions, where abundant data exist, with the structure of liquids, where measurements of structure are relatively scarce. Because glass at ambient conditions is typically denser than the 1 bar liquid, we would expect the structure of glass to reflect the structure of the liquid at slightly elevated pressure. In

Table 3
FPMD results as a function of temperature T and volume V for the pressure P, internal energy E, enthalpy $H = E + PV$, and electronic entropy S_{el}.

T (K)	V (cm^3 mol^{-1})	P (GPa)	E (kJ mol^{-1})	H (kJ mol^{-1})	S_{el} (J mol^{-1} K^{-1})
2000	70.048	6.31 ± 1.43	−7054.23 ± 17.49	−6611.89 ± 101.68	0.01 ± 0.00
2000	77.831	2.23 ± 1.50	−7070.56 ± 11.05	−6897.09 ± 117.45	0.01 ± 0.00
2000	81.800	1.44 ± 1.44	−7064.00 ± 16.14	−6946.45 ± 119.18	0.01 ± 0.00
3000	46.698	70.03 ± 1.61	−6426.67 ± 14.66	−3156.29 ± 75.39	0.27 ± 0.01
3000	54.481	34.08 ± 1.54	−6661.97 ± 11.75	−4805.13 ± 83.94	0.52 ± 0.04
3000	62.265	17.53 ± 1.45	−6729.09 ± 11.89	−5637.84 ± 90.14	1.04 ± 0.04
3000	70.048	9.37 ± 1.46	−6758.96 ± 13.40	−6102.40 ± 102.54	1.70 ± 0.12
3000	77.831	5.00 ± 1.43	−6780.56 ± 8.53	−6391.25 ± 110.92	1.74 ± 0.06
3000	81.800	3.17 ± 1.44	−6767.79 ± 7.96	−6508.24 ± 117.62	2.06 ± 0.12
4000	38.915	160.04 ± 1.55	−5492.81 ± 21.57	735.31 ± 62.21	0.83 ± 0.10
4000	46.698	76.91 ± 1.44	−6120.26 ± 16.68	−2528.69 ± 68.12	1.56 ± 0.07
4000	54.481	40.42 ± 1.45	−6297.82 ± 13.44	−4095.57 ± 79.20	3.87 ± 0.22
4000	62.265	21.81 ± 1.45	−6398.88 ± 10.53	−5040.70 ± 90.35	5.22 ± 0.16
4000	70.048	12.09 ± 1.45	−6408.17 ± 18.66	−5561.36 ± 102.65	6.55 ± 0.39
4000	77.831	6.88 ± 1.43	−6404.72 ± 19.22	−5869.63 ± 112.03	7.27 ± 0.43
4000	81.800	4.86 ± 1.44	−6408.47 ± 13.19	−6010.92 ± 117.63	7.73 ± 0.25
6000	38.915	178.61 ± 1.50	−4784.08 ± 27.45	2166.47 ± 73.28	7.59 ± 0.75
6000	46.698	93.07 ± 1.51	−5349.80 ± 17.55	−1003.58 ± 71.15	12.01 ± 0.33
6000	54.481	51.78 ± 1.43	−5550.10 ± 19.08	−2729.11 ± 79.47	16.99 ± 0.39
6000	62.265	30.29 ± 1.45	−5605.39 ± 16.70	−3719.27 ± 90.85	21.19 ± 0.37
6000	70.048	18.49 ± 1.43	−5618.48 ± 20.32	−4323.23 ± 101.50	23.90 ± 0.51
6000	77.831	11.90 ± 1.45	−5605.77 ± 12.27	−4679.66 ± 112.39	26.45 ± 0.31
6000	81.800	9.08 ± 1.53	−5571.35 ± 15.78	−4828.61 ± 118.44	28.25 ± 0.51

Table 4
Thermodynamic properties of diopside liquid at 0 GPa and 1773 K.

	FPMD	Experiment
V_0 (cm^3 mol^{-1})	82.90 (14)	82.64 (10)[a]
K_T (GPa)	18.0 (2)	20.4 (1)[b]
K_S (GPa)	20.1 (3)	24.2[c]
K'	6.04 (11)	6.9[d], 6.98[e]
α (10^{-6} K^{-1})	124.5 (30)	86 (3)[a]
C_V (Nk)	4.37 (10)	4.08 (6)[f]
γ	0.51 (5)	0.42 (2)[g]

References: (a) Lange (1997), (b) Ai and Lange (2008), (c) Rivers and Carmichael (1987), (d) Rigden et al. (1989), (e) Asimow and Ahrens (2010), (f) Stebbins et al. (1984) and (g) computed from the other experimental quantities given.

the case of diopside, the difference is subtle and comparable to experimental resolution of structural parameters as the difference in density between the liquid at the 1 bar melting point and the glass at ambient conditions is only 5%. The expected subtlety of the difference is consistent with the agreement that we find, within uncertainty, for the values of Q^n and k_n between our liquid and experimental measurements on the glass (Table 1).

The variation of the Si–O coordination distribution on compression reveals a fundamentally important aspect of silicate liquid structure (Fig. 2). Fivefold Si–O coordination is most abundant in the liquid at intermediate compressions. This contrasts with the structure of silicate crystals in which fivefold coordination is extremely rare. Silicate liquid structure then cannot be considered to be a somewhat disordered version of crystalline structure; the differences are more profound. The pre-dominance of fivefold coordination at intermediate compression has at least two important consequences: (1) it contributes to the gradual change in the mean Si–O coordination number and the density with increasing pressure. (2) Fivefold coordination has been proposed as an essential transition state facilitating diffusion and viscous flow (Angell et al., 1982). Indeed experiments on diopside liquid show an initial decrease in viscosity with increasing pressure, consistent with the growth of fivefold coordination (Reid et al., 2003). Fivefold coordinated Si has also been seen experimentally in glasses quenched from liquids at elevated pressure (Stebbins, 1991), although in smaller proportions than we find in our simulations of in situ liquid.

The increase in the mean Si–O coordination on compression is smooth and monotonic (Fig. 1). For $V/V_X < 0.95$ the increase in mean coordination number is nearly linear in the volume. The evolution of liquid structure that we find therefore contrasts with speciation models that explicitly partition compression among a small number of assumed structural states (4-, 5-, and 6-fold Si–O coordination) (Ghiorso, 2004). Speciation models tend to produce "wavy" equations of state in which the compressibility can vary non-monotonically with pressure, behavior that we do not see. Only at the largest volumes does it appear that homogeneous fourfold coordination is preferred as the Si–O coordination number is nearly constant for $V/V_X > 0.95$. The prevalence of fourfold coordination at large volume is consistent with theory and experiment on silica aerogels and ruptured silica glass which show nearly perfect tetrahedral coordination at densities less than half that of the liquid at the ambient melting point (Kieffer and Angell, 1988; Bhattacharya and Kieffer, 2005). The variation of

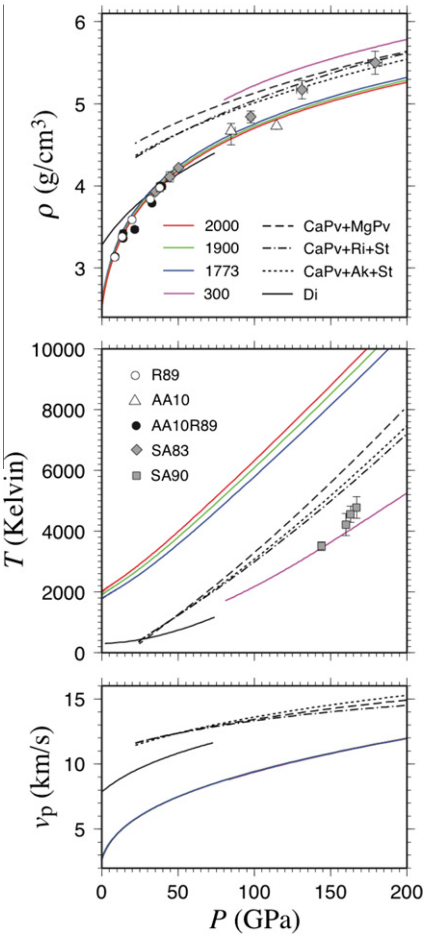

Fig. 4. Properties of $CaMgSi_2O_6$ liquid along the Hugoniot computed from our thermodynamic fundamental relation (colored solid lines) compared with experimental measurements as indicated (symbols) and (black solid and black dashed lines) the Hugoniot of crystalline assemblages as indicated computed from the model of (Xu et al., 2008) (CaPv: $CaSiO_3$ perovksite, MgPv: $MgSiO_3$ perovskite, ri: Mg_2SiO_4 ringwoodite, st: SiO_2 stishovite, Ak: $MgSiO_3$ akimotoite). Curves are computed assuming a liquid initial state and initial (uncompressed) temperatures of 1773 K (blue), 1900 K (green), and 2000 K (red); and assuming a crystalline diopside initial state and an uncompressed temperature of 300 K (purple, black solid, and black dashed lines). Note that red, blue, and green curves nearly coincide in the case of the v_P. Experimental data is from R89 (Rigden et al., 1989); AA10 (Asimow and Ahrens, 2010); AA10R89: (Asimow and Ahrens, 2010) re-interpretation of (Rigden et al., 1989); SA83 (Svendsen and Ahrens, 1983); and SA90 (Svendsen and Ahrens, 1990). (For interpretation of the references to colour in this figure legend, the reader is referred to the web version of this article.)

the mean Si–O coordination number and the proportion of oxygen tri-clusters on compression is broadly consistent with spectroscopic studies of $MgSiO_3$ and $CaMgSi_2O_6$ glass compressed at ambient temperature (Williams and Jeanloz, 1988; Lee et al., 2008). A detailed comparison however is impossible because these spectroscopic probes are not quantified. Exploratory *in situ* X-ray diffraction data in $MgSiO_3$ and $CaSiO_3$ liquids shows an increase in the mean

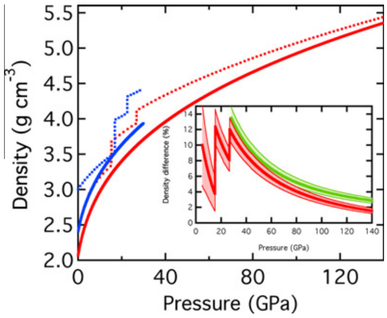

Fig. 5. Density of liquid (solid lines) and equilibrium crystalline assemblages (dashed lines) of diopside composition at 4000 K (red) and 2428 K (blue). Inset shows the density difference between liquid and crystalline assemblages at 4000 K for diopside (red) and enstatite (green) compositions. The density of the equilibrium crystalline assemblage is computed from the model of Xu et al. (2008). (For interpretation of the references to colour in this figure legend, the reader is referred to the web version of this article.)

Si–O coordination number with increasing pressure that is consistent with our findings (Funamori et al., 2004).

Our results lend additional insight into widely used approximations to density functional theory: LDA and GGA. Physically, these two approximations to the exchange-correlation functional differ in that in LDA the exchange-correlation functional depends on the local charge density, whereas in GGA, it also depends on local charge density gradients. As GGA is more elaborate, while sharing with LDA the advantages of being parameter free and of satisfying exact sum rules of the exchange correlation functional, it has been described as the next rung on a "Jacob's Ladder" towards the paradise of chemical accuracy (Perdew and Schmidt, 2001). However, GGA does not always yield more accurate predictions. Indeed, in our work we have focused on LDA because it predicts more accurately than GGA the equation of state and physical properties of crystalline silicates (Karki et al., 2001). On the other hand, LDA is also known to yield less accurate predictions of the relative energetics of crystalline phases. For example, LDA predicts stishovite to be the ground state of SiO_2, whereas GGA correctly predicts quartz to be the ground state (Hamann, 1996). If this difference reflects the tendency of LDA and GGA to stabilize different coordination environments (tetrahedral versus octahedral) to different degrees, then we might expect LDA and GGA to predict very different liquid structure at the same volume. However, this is not what we see: LDA and GGA predict the same Si–O coordination number (Fig. 1).

The near identity of liquid structure predicted by LDA and GGA is remarkable in the context of previous comparisons between these two approximations in crystalline systems. Our interpretation is that finite temperature, and attendant structural disorder, plays an important role through its tendency to homogenize the charge density. While others have also emphasized the role of temperature in evaluating the accuracy of approximations to density functional theory(Faleev et al., 2006), albeit in very different systems, our interpretation must be regarded as tentative as there have been remarkably few careful comparisons between LDA and GGA at elevated temperature.

Our results support the notion that the LDA error can be corrected to a good approximation by the addition of a small correction P_{xc} that depends only on chemical composition, and that is independent of volume, temperature, or structure (van de Walle and Ceder, 1999). The same value of P_{xc} that yields, by definition, perfect agreement with the volume of crystalline diopside, also produces excellent agreement with measurements of the zero pressure volume of diopside liquid and its Hugoniot. The notion of P_{xc} in the context of GGA is more problematic. First P_{xc} for GGA is more than twice as large in magnitude that P_{xc} for LDA (although still small on the scale of the pressure range investigated here), reflecting inferior GGA predictions of physical properties of oxides and silicates. Second, the GGA error apparently depends sensitively on structure: the value of P_{xc} that yields, by definition, good agreement with the volume of crystalline diopside, fails to yield agreement with the zero pressure volume of diopside liquid.

The equation of state of the liquid differs fundamentally from all known crystalline silicate equations of state. The Grüneisen parameter increases on compression rather than decreases as in crystals (Stixrude and Lithgow-Bertelloni, 2005) (Fig. 3). The change is substantial: nearly a factor of 3 on twofold compression. Similar behavior is seen in all the liquids that we have studied to date, including $MgSiO_3$, Mg_2SiO_4, MgO, SiO_2, and $CaAl_2Si_2O_8$ (Stixrude and Karki, 2005; Karki et al., 2006, 2007; de Koker et al., 2008; de Koker, 2010). We have argued that the increase in the Grüneisen parameter on compression is related to the increase in coordination number: the liquid appears to track the increase in γ on going from low-pressure to high-pressure crystalline polymorphs (Stixrude and Karki, 2005). This apparently universal feature of silicate liquids is important because the Grüneisen parameter controls the isentropic gradient via

$$\left(\frac{\partial \ln T}{\partial P}\right)_s = \frac{\gamma}{K_s} \tag{17}$$

the large value of γ at high pressure means that the isentropes of magma oceans are much hotter than previously thought, with important implications for their evolution (Stixrude et al., 2009).

The density contrast between diopside composition liquid and the isochemical crystalline assemblage is less than that between $MgSiO_3$ liquid and $MgSiO_3$ perovskite at the base of the mantle (Stixrude and Karki, 2005). In the case of $MgSiO_3$, we argued that partitioning of Fe into the liquid may be sufficient to make the liquid denser than coexisting solids in the multi-component mantle. Our results here indicate that addition of Ca to the system will further enhance the density of the liquid relative to the solid, making crystal-liquid density inversion just above the core-mantle boundary even more likely.

5. CONCLUSIONS

The good agreement that we find between density functional theory and experiment here is particularly important as diopside composition has been more widely studied experimentally at high pressure than any other system that we have examined to date. Agreement between our predictions and recent shock wave measurements at mid lower-mantle conditions is especially gratifying and points to density functional theory as a powerful tool for exploring the physics and chemistry of silicate liquids at extreme conditions. At the same time first principles molecular dynamics simulations are able to provide insight into the relationship between structure and thermodynamic properties at a level that will likely remain challenging experimentally.

Among the unexpected and geophysically significant properties of silicate liquids at very high pressure are the large value of the Grüneisen parameter and the small isochemical liquid–solid density contrast, which decreases upon replacement of Mg for Ca. Such properties will form a basis for any discussion of the dynamics and consequences of melts in the deep Earth including in deep magma oceans. Indeed, models of deep magma oceans are still in their infancy (Labrosse et al., 2007), and substantial progress, based on improved knowledge of silicate liquid properties can be expected.

ACKNOWLEDGMENTS

This research was supported by the National Science Foundation under Grants EAR-0409074 and EAR-0409121, and the National Environmental Research Council under Grant NE/F017871. Computing facilities were provided by CCT at Louisiana State University.

REFERENCES

Ai Y. H. and Lange R. A. (2008) New acoustic velocity measurements on CaO–MgO–Al_2O_3–SiO_2 liquids: reevaluation of the volume and compressibility of $CaMgSi_2O_6$–$CaAl_2Si_2O_8$ liquids to 25 GPa. *J. Geophys. Res. – Solid Earth* **113**, B04203.

Angell C. A., Cheeseman P. A. and Kadiyala R. R. (1987) Diffusivity and thermodynamic properties of diopside and jadeite melts by computer-simulation studies. *Chem. Geol.* **62**, 83–92.

Angell C. A., Cheeseman P. A. and Tamaddon S. (1982) Pressure enhancement of ion mobilities in liquid silicates from computer-simulation studies to 800-Kilobars. *Science* **218**, 885–887.

Asimow P. D. and Ahrens T. J. (2010) Shock compression of liquid silicates to 125 GPa: the anorthite–diopside join. *J. Geophys. Res.* **115**, B10209.

Atkins P. W. (1994) *Physical Chemistry*. Freeman, New York.

Bhattacharya S. and Kieffer J. (2005) Fractal dimensions of silica gels generated using reactive molecular dynamics simulations. *J. Chem. Phys.* **122**, 094715.

Canup R. M. (2004) Dynamics of lunar formation. *Annu. Rev. Astron. Astrophys.* **42**, 441–475.

Car R. and Parrinello M. (1985) Unified approach for molecular dynamics and density–functional theory. *Phys. Rev. Lett.* **55**, 2471–2474.

Ceperley D. M. and Alder B. J. (1980) Ground state of the electron gas by a stochastic method. *Phys. Rev. Lett.* **45**, 566–569.

de Koker N. (2010) Structure, thermodynamics, and diffusion in $CaAl_2Si_2O_8$ liquid from first-principles molecular dynamics. *Geochim. Cosmochim. Acta* **74**, 5657–5671.

de Koker N. and Stixrude L. (2009) Self-consistent thermodynamic description of silicate liquids, with application to shock melting of MgO periclase and $MgSiO_3$ perovskite. *Geophys. J. Int.* **178**, 162–179.

de Koker N. and Stixrude L. (2010) Self-consistent thermodynamic description of silicate liquids, with application to shock melting of MgO periclase and $MgSiO_3$ perovskite (vol. 178, p. 162, 2009). *Geophys. J. Int.* **183**, 478.

de Koker N. P., Stixrude L. and Karki B. B. (2008) Thermodynamics, structure, dynamics, and freezing of Mg_2SiO_4 liquid at high pressure. *Geochim. Cosmochim. Acta* **72**, 1427–1441.

Faleev S. V., van Schilfgaarde M., Kotani T., Leonard F. and Desjarlais M. P. (2006) Finite-temperature quasiparticle self-consistent GW approximation. *Phys. Rev. B* **74**, 033101.

Francis G. P. and Payne M. C. (1990) Finite basis set corrections to total-energy pseudopotential calculations. *J. Phy. – Condens. Matter* **2**, 4395–4404.

Funamori N., Yamamoto S., Yagi T. and Kikegawa T. (2004) Exploratory studies of silicate melt structure at high pressures and temperatures by in situ X-ray diffraction. *J. Geophys. Res. – Solid Earth* **109**, B03203.

Gasparik T. (1996) Melting experiments on the enstatite–diopside join at 70–224 kbar, including the melting of diopside. *Contrib. Mineral. Petrol.* **124**, 139–153.

Ghiorso M. S. (2004) An equation of state for silicate melts. III. Analysis of stoichiometric liquids at elevated pressure: Shock compression data, molecular dynamics simulations and mineral fusion curves. *Am. J. Sci.* **304**, 752–810.

Haggerty S. E. and Sautter V. (1990) Ultradeep (Greater Than 300 Kilometers), Ultramafic Upper Mantle Xenoliths. *Science* **248**, 993–996.

Hamann D. R. (1996) Generalized gradient theory for silica phase transitions. *Phys. Rev. Lett.* **76**, 660–663.

Herzberg C. (1995) Generation of plume magmas through time – an experimental perspective. *Chem. Geol.* **126**, 1–16.

Karki B. B., Bhattarai D. and Stixrude L. (2006) First-principles calculations of the structural, dynamical, and electronic properties of liquid MgO. *Phys. Rev. B* **73**, 174208.

Karki B. B., Bhattarai D. and Stixrude L. (2007) First-principles simulations of liquid silica: structural and dynamical behavior at high pressure. *Phys. Rev. B* **76**, 104205.

Karki B. B., Stixrude L. and Wentzcovitch R. M. (2001) High-pressure elastic properties of major materials of Earth's mantle from first principles. *Rev. Geophys.* **39**, 507–534.

Kieffer J. and Angell C. A. (1988) Generation of fractal structures by negative-pressure rupturing of SiO_2 glass. *J. Non-Cryst. Solids* **106**, 336–342.

Kohn W. (1999) Nobel lecture: electronic structure of matter-wave functions and density functionals. *Rev. Mod. Phys.* **71**, 1253–1266.

Kresse G. and Furthmuller J. (1996) Efficient iterative schemes for ab initio total-energy calculations using a plane-wave basis set. *Phys. Rev. B* **54**, 11169–11186.

Kresse G., Hafner J. and Needs R. J. (1992) Optimized norm-conserving pseudopotentials. *J. Phys. – Condens. Matter* **4**, 7451–7468.

Labrosse S., Hernlund J. W. and Coltice N. (2007) A crystallizing dense magma ocean at the base of the Earth's mantle. *Nature* **450**, 866–869.

Lange R. A. (1997) A revised model for the density and thermal expansivity of K_2O–Na_2O–CaO–MgO–Al_2O_3–SiO_2 liquids from 700 to 1900 K: extension to crustal magmatic temperatures. *Contrib. Mineral. Petrol.* **130**, 1–11.

Lee S. K., Lin J. F., Cai Y. Q., Hiraoka N., Eng P. J., Okuchi T., Mao H. K., Meng Y., Hu M. Y., Chow P., Shu J. F., Li B. S., Fukui H., Lee B. H., Kim H. N. and Yoo C. S. (2008) X-ray Raman scattering study of $MgSiO_3$ glass at high pressure: implication for triclustered $MgSiO_3$ melt in Earth's mantle. *Proc. Natl. Acad. Sci. USA* **105**, 7925–7929.

Matsui M. (1996) Molecular dynamics simulation of structures, bulk moduli, and volume thermal expansivities of silicate liquids in the system CaO–MgO–Al_2O_3–SiO_2. *Geophys. Res. Lett.* **23**, 395–398.

McQuarrie D. A. (1976) *Statistical Mechanics*. Harper and Row, New York.

Mermin N. D. (1965) Thermal properties of inhomogeneous electron gas. *Phys. Rev.* **137**, A1441–A1443.

Miller G. H., Stolper E. M. and Ahrens T. J. (1991) The equation of state of a Molten Komatiite.1. Shock-wave compression to 36 GPa. *J. Geophys. Res. – Solid Earth and Planets* **96**, 11831–11848.

Mookherjee M., Stixrude L. and Karki B. (2008) Hydrous silicate melt at high pressure. *Nature* **452**, 983–986.

Nosé S. (1984) A unified formulation of the constant temperature molecular–dynamics methods. *J. Chem. Phys.* **81**, 511–519.

Oganov A. R., Brodholt J. P. and Price G. D. (2001) Ab initio elasticity and thermal equation of state of $MgSiO_3$ perovskite. *Earth Planet. Sci. Lett.* **184**, 555–560.

Perdew J. P. and Schmidt K. (2001) Jacob's ladder of density functional approximations for the exchange-correlation energy. In *Density Functional Theory and Its Applications to Materials* (eds. V. E. Van Doren, K. Van Alsenoy and P. Geerlings). American Institute of Physics, New York, pp. 1–20.

Ralchenko Y., Kramida A. E., Reader J. and Team N. A. (2010) *NIST Atomic Spectra Database (version 3.1.5)*. National Institute of Standards and Technology, Gaithersburg, MD. <http://physics.nist.gov/asd3>

Reid J. E., Suzuki A., Funakoshi K. I., Terasaki H., Poe B. T., Rubie D. C. and Ohtani E. (2003) The viscosity of $CaMgSi_2O_6$ liquid at pressures up to 13 GPa. *Phys. Earth Planet. In.* **139**, 45–54.

Rigden S. M., Ahrens T. J. and Stolper E. M. (1989) High-pressure equation of state of molten anorthite and diopside. *J. Geophys. Res.* **94**, 9508–9522.

Rivers M. L. and Carmichael I. S. E. (1987) Ultrasonic Studies Of Silicate Melts. *J. Geophys. Res. – Solid Earth and Planets* **92**, 9247–9270.

Schneider J., Mastelaro V. R., Panepucci H. and Zanotto E. D. (2000) Si-29 MAS-NMR studies of Q(n) structural units in metasilicate glasses and their nucleating ability. *J. Non-Cryst. Solids* **273**, 8–18.

Stebbins J. F. (1987) Identification of multiple structural species in silicate-glasses by Si-29 NMR. *Nature* **330**, 465–467.

Stebbins J. F. (1991) NMR evidence for 5-coordinated silicon in a silicate glass at atmospheric-pressure. *Nature* **351**, 638–639.

Stebbins J. F., Carmichael I. S. E. and Moret L. K. (1984) Heat-capacities and entropies of silicate liquids and glasses. *Contrib. Mineral. Petrol.* **86**, 131–148.

Stixrude L., de Koker N., Sun N., Mookherjee M. and Karki B. B. (2009) Thermodynamics of silicate liquids in the deep Earth. *Earth Planet. Sci. Lett.* **278**, 226–232.

Stixrude L. and Karki B. (2005) Structure and freezing of $MgSiO_3$ liquid in Earth's lower mantle. *Science* **310**, 297–299.

Stixrude L. and Lithgow-Bertelloni C. (2005) Thermodynamics of mantle minerals - I. Physical properties. *Geophys. J. Int.* **162**, 610–632.

Svendsen B. and Ahrens T. J. (1983) Dynamic compression of diopside and salite to 200 GPa. *Geophys. Res. Lett.* **10**, 501–504.

Svendsen B. and Ahrens T. J. (1990) Shock-induced temperatures of Camgsi2o6. *J. Geophys. Res. – Solid Earth and Planets* **95**, 6943–6953.

van de Walle A. and Ceder G. (1999) Correcting overbinding in local-density-approximation calculations. *Phys. Rev. B* **59**, 14992–15001.

Vorberger J., Tamblyn I., Militzer B. and Bonev S. A. (2007) Hydrogen–helium mixtures in the interiors of giant planets. *Phys. Rev. B* **75**, 024206.

Wan J. T. K., Duffy T. S., Scandolo S. and Car R. (2007) First-principles study of density, viscosity, and diffusion coefficients of liquid $MgSiO_3$ at conditions of the Earth's deep mantle. *J. Geophys. Res. – Solid Earth* **112**, B03208.

Waseda Y. and Toguri J. M. (1977) Structure of molten binary silicate systems CaO–SiO_2 and MgO–SiO_2. *Metall. Trans. B* **8**, 563–568.

Wentzcovitch R. M., Martins J. L. and Allen P. B. (1992) Energy versus free-energy conservation in 1st-principles molecular-dynamics. *Phys. Rev. B* **45**, 11372–11374.

Williams Q. and Garnero E. J. (1996) Seismic evidence for partial melt at the base of Earth's mantle. *Science* **273**, 1528–1530.

Williams Q. and Jeanloz R. (1988) Spectroscopic evidence for pressure-induced coordination changes in silicate-glasses and melts. *Science* **239**, 902–905.

Xu W. B., Lithgow-Bertelloni C., Stixrude L. and Ritsema J. (2008) The effect of bulk composition and temperature on mantle seismic structure. *Earth Planet. Sci. Lett.* **275**, 70–79.

Zhang L. Q., Van Orman J. A. and Lacks D. J. (2010) Molecular dynamics investigation of MgO–CaO–SiO_2 liquids: influence of pressure and composition on density and transport properties. *Chem. Geol.* **275**, 50–57.

Associate editor: Peter Ulmer